BIOMATERIALS SYNTHESIS AND CHARACTERIZATION

Original Research

Enhanced osteogenesis properties of titanium implant materials by highly uniform mesoporous thin films of hydroxyapatite and titania intermediate layer

Fatemeh Jalali[1] · Hamid Oveisi [1,2] · Azadeh Meshkini[3,4]

Abstract

Titanium (Ti) has been widely used for medical and dental applications; however, bare Ti cannot be properly connected to a living bone, and hence some modifications are needed for this purpose. The present study describes the synthesis of mesoporous hydroxyapatite thin films (MHF) on titanium implant materials for speeding up and shortening the processes of osteointegration. The uniform MHF was coated on a Ti substrate following the insertion of intermediate titania (TiO_2) film via the sol–gel dip-coating method. The intermediate titania layer improved the bonding strength between the MHF and Ti substrate. MHFs were synthesized using a precursor solution containing phosphoric acid, calcium nitrate tetrahydrate, and a nonionic surfactant ($C_{12}E_{10}$) as the phosphate source, calcium source, and structure-directing agent, respectively. The effect of calcination temperature on phase composition, morphology, microstructure, roughness, and wettability of the MHFs was investigated using XRD, FE-SEM, COM, AFM, and contact angle measurement. The XRD results revealed the crystalline hydroxyapatite phase, which was improved with an increase in the calcination temperature. Moreover, the FE-SEM images showed the crack-free MHFs, uniform thickness of the layer, and mesoporous surface morphology. In addition, it was found that the roughness and wettability of the samples change upon the alteration of calcination temperature. The biological studies demonstrated that MHFs support the adhesion and proliferation of the mesenchymal stem cells (MSCs) and guid them toward osteogenic differentiation. Therefore, the MHFs prepared in this study may be useful in a wide range of applications, particularly in bone regeneration medicine.

Graphical Abstract
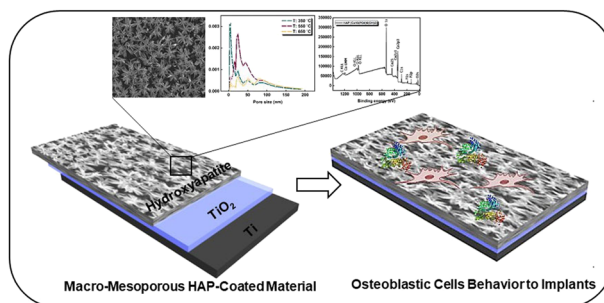
✉ Hamid Oveisi
Hamid.Oveisi@hsu.ac.ir

1   Department of Materials and Polymer Engineering, Hakim Sabzevari University, Sabzevar 9617976487, Iran

2   Nanotechnology Research Center, Hakim Sabzevari University, Sabzevar 9617976487, Iran

3   Faculty of Science, Department of Chemistry, Ferdowsi University of Mashhad, Mashhad 9177948974, Iran

4   The Research Institute of Biotechnology, Ferdowsi University of Mashhad, Mashhad 9177948974, Iran

1 Introduction

Recently, mesoporous materials have attracted particular attention owing to their high surface area, tunable pore size, and large pore volume. These properties make mesoporous materials suitable for application in various areas such as biomaterials, catalysts, adsorbents, drug delivery systems. Therefore, synthesis of mesoporous materials has been an area of great scientific interest [1–7].

Mesoporous biomaterials are synthesized by means of surfactant-assisted methods or templating techniques [8–10]. Studies have demonstrated that the porosity of a biomaterial can promote the natural bone-forming ability and direct bonding to host bones [11, 12]. Among these materials, hydroxyapatite with the structural formula of $Ca_{10}(PO_4)_6$ $(OH)_2$ has been proved as one of the most important bioceramics in medical and dental applications thanks to its high biocompatibility, ability to form a chemical bond with living bone tissues, suitable osteoconductivity, nontoxic properties, and a similar structure to the natural bone mineral [13–17]. According to the wide applications of hydroxyapatite, various morphologies have been reported [13, 18, 19]. Among various morphologies of hydroxyapatite, thin-film morphology has attracted more attention for applications in bone and tooth repair as it enhances the biocompatibility and accelerates the process of ossification [20, 21].

However, an important challenge with hydroxyapatite thin films is related to the low mechanical strength of these films as load-bearing implants. To overcome this problem, mesoporous hydroxyapatite films (MHFs) are often coated on metal material supports such as titanium (Ti), stainless steel, and Ti-based alloys that have good mechanical properties [22, 23]. These metal materials have been used as an implant in dental and orthopedic applications. Among them, Ti is biocompatible and besides, it does not release metallic ions, such as Fe, Ni, Al, and V; therefore, it is a better candidate for biomedical applications. However, despite its advantages, its ability to bond to the host cells upon implantation is weak. In order to improve the bone-bonding ability, its surface should be modified [21]. To do so, various methods have been used [24]. Many studies have demonstrated that hydroxyapatite-coated Ti implants have a higher bone-bonding ability and earlier osteoid formation than the Ti uncoated implant [25–27].

Therefore, mesoporous hydroxyapatite thin-film coating on Ti substrate simultaneously provides excellent biocompatibility of hydroxyapatite and load-bearing ability of Ti substrate. However, the main drawbacks of the hydroxyapatite coating such as the low bond strength and high residual stress lead to the separation of hydroxyapatite from the surface of the implant during long-term in vivo applications. This phenomenon causes inflammatory responses in the physiological environment [14]. To address this issue, a wide range of substrate's surface treatments has been implemented [28, 29]. In this line, some researchers have used a transition layer such as metal oxides (e.g., TiO_2 and ZrO_2) between substrate and hydroxyapatite coating, resulting in strength and stability enhancement of hydroxyapatite coating [30–32]. In addition, the intermediate layer on Ti substrate has been used to improve the corrosion resistance of Ti. Among metal oxides, TiO_2 as an intermediate layer between hydroxyapatite coating and Ti substrate is more favorable owing to the high mechanical integrity of TiO_2 with hydroxyapatite, chemical similarity to both HA and titanium, outstanding tribological properties, biocompatibility, and antibacterial properties [33–38]. Different methods are employed for the coating of Ti substrate with titania [39, 40]. Among them, the sol–gel technique is an ideal way to create thin films, owing to the phase homogeneity of the films, fine grain structure, low processing temperature, and effective production of the film on complex-shaped implants [26, 31, 41–43].

In this research, we report the synthesis of hydroxyapatite-titania double-layer coating on Ti substrate. The titania thin film between the hydroxyapatite coating and Ti substrate is designed to improve the bonding capability and adhesive properties of the hydroxyapatite on the surface of the Ti substrate. The MHF was developed via the sol–gel dip-coating method using a nonionic surfactant as a template. In order to investigate the mesoporous hydroxyapatite thin films (MHFs) microstructure, phase composition, morphology, roughness, and wettability, XRD, FE-SEM, confocal optical microscope (COM), AFM, and contact angle measurement were utilized. To investigate the biological behaviors of the fabricated samples, the protein adsorption on the surface of samples was evaluated. Osteogenesis induced by MHFs in the mesenchymal stem cells (MSCs) was characterized by a sequence of events, involving cell attachment and proliferation, and it was followed by the activity of alkaline phosphatase. It is expected that the prepared hydroxyapatite films on the surface of implant improve the bioactivity of metal implants for prospective applications.

2 Experimental details

2.1 Chemical materials

The calcium nitrate tetrahydrate $(Ca(NO_3)_2.4H_2O$, Merck) and phosphoric acid $(H_3PO_4$, Merck, 85%) as calcium and phosphorous precursors, respectively, were utilized to prepare the sol solution. The nonionic surfactant decaethylene glycol monododecyl ether $(C_{12}H_{25}(OCH_2CH_2)_{10}OH$, $C_{12}E_{10})$ was purchased from Sigma-Aldrich Co. and used

without any purification. Titanium (IV) tetra-isopropoxide (TTIP, Sigma-Aldrich, 97%), hydrochloric acid (HCl, Merck, 37%), and absolute ethanol (Carlo Erba) were used for the preparation of TiO_2 solution.

2.2 Substarte preparation

A commercially pure titanium sheet with 2-mm thickness (grade 2) was used as a substrate for the intermediate layer and hydroxyapatite coating. The titanium sheet was cut into pieces with 10×20 mm dimensions. The substrates were sanded using sandpaper No. 120–1000 and polished using alumina solution. Then, the substrates were placed in a beaker containing acetone and cleaned under the ultrasonic condition for 30 min. Finally, the substrates were washed with ethanol solution three times and dried in an oven for 10 min.

2.3 Titania intermediate layer

For the preparation of TiO_2 sol solution, HCl (35 wt%) was added to titanium TTIP dropwise and stirred vigorously at room temperature for 5 min. Then, the specified amount of absolute ethanol was added to the solution. The final molar ratio of the chemical materials was as follows: TTIP:HCl: EtOH, 1.000:5.487:29.324. The final solution was aged under mild stirring at room temperature for 20 h to obtain a clear sol. The dip-coating method was used for titania coating on Ti substrate. While the substrate was pulled out with a speed of 1 cm min^{-1} from the solution, the thin-film coating started to be deposited on it. The thickness of the coating was directly adjusted by pulling out speed. The coated substrates were then heat-treated in the furnace at 500 °C temperature for 2 h.

2.4 Synthesis of mesoporous hydroxyapatite-titania double-layer coating on Ti substrate (MHFs)

For the preparation of hydroxyapatite sol, $C_{12}E_{10}$ was added to ultrapure deionized water (7.000 ml) in a vial and stirred for 30 min to get homogenized solution. The calcium nitrate was added and stirred for another 30 min. Then, the required amount of phosphoric acid was added to the final solution. After adjusting the pH by different amounts of aqueous ammonia at 0, 0.65, 2, 7, and 10, the final solution was aged under mild stirring at room temperature for 24 h. The final molar ratio of the precursor sol was as follows: $C_{12}E_{10}$:Ca(NO$_3$)$_2$.4H$_2$O:H$_3$PO$_4$, 1.000:5.013:3.007. Dip-coating method with a speed of 1 cm min^{-1} was applied to obtain uniform hydroxyapatite thin layer on TiO$_2$-coated implants. The as-made thin films were calcined at three different temperatures 350, 500, and 650 °C for 2 h and named as MHF350, MHF500, and MHF650, respectively.

2.5 Characterization

The XRD patterns of the materials were recorded in the 2θ range from $10°$ to $70°$ by a continuous scanning mode (0.02°/min) on a Rigaku-SmartLab X-ray diffractometer with CuKα radiation ($\lambda = 0.154$ nm). The crystallite size was calculated by the Debye–Scherrer Eq. (1). The Debye–Scherrer equation is:

$$D = K \cdot \lambda / (\beta \cdot cos\theta) \tag{1}$$

where D is the mean crystallite size, K is the shape factor of the crystallites ($k = 0.9$), λ is the wavelength of the incident X-ray ($\lambda = 0.154$ nm), β is the full width at half-maximum, and θ is the peak position. The functional groups of the films were studied by Fourier-transform infrared spectroscopy (FTIR). The FTIR spectrum was collected in the range 400–4000 cm^{-1}. For the purpose of FTIR analysis, the films were scratched from the surface of the titanium substrate and the standard KBr pellet was made. To investigate the mesostructural parameters of thin films, nitrogen adsorption–desorption analysis was performed. For the purpose of nitrogen adsorption–desorption analysis, the films were scratched from the surface of the substrate and were degassed at 353 K for 24 h prior to the nitrogen adsorption measurements. The specific surface area was determined by the Bruaauer–Emmett–Teller (BET) method. The pore volume and pore diameter were evaluated based on the Barrett–Joyner–Halenda (BJH) model. The surface morphology, cross-section, elemental distribution, and mapping of the films were evaluated with a field-emission scanning electron microscope (FE-SEM, TESCAN Mira 3-XMU). In order to investigate the surface topography and roughness of the films, atomic force microscopy (AFM, SOLVER NEXT, NT-MDT, Russia) was employed. The surface properties of the coating were studied by the COM. The chemical state of the components of the film was studied by X-ray photoelectron spectroscopy (XPS) technique. The XPS was performed at room temperature using a JPS-9010TR (JEOL) instrument with an MgKα X-ray source. All binding energies were calibrated by referencing to C1s (285.0 eV).

2.6 Protein adsorption

Bovine serum albumin (BSA) with molecular weight 66.5 kDa and an isoelectric point 4.7 was used for the protein adsorption study. For the assessment of protein adsorption on the surface of the MHF materials, they were immersed in the BSA solution (200 µg ml^{-1}) at 37 °C. At different times (interval 2–72 h), the amount of protein loaded on the surface of fabricated materials was quantified by determining protein concentration reduction in the supernatant, which was analyzed by the Bradford method [44].

2.7 Cell proliferation assay

The human MSCs obtained from the Research Institute of Biotechnology (Mashhad, Iran) were cultured in DMEM (Dulbecco's modified Eagle's medium) supplemented with glucose (1000 mg l^{-1}), FBS (10%, v/v), streptomycin (100 µg ml^{-1}), and penicillin (100 U ml^{-1}). The cells were incubated under 5% CO$_2$ humidified atmosphere at 37 °C. To evaluated cell proliferation, the cells were seeded in six-well tissue culture plates containing the fabricated materials (Ti substrate, MHF500, or MHF650) with a density of 2×10^5 cells. After 7 days, the materials were transferred to another six-well tissue culture plates and trypsinized. Then, the cell number was determined using a hemocytometer and the abilities of the cells to exclude trypan blue.

2.8 Alkaline phosphatase activity

To evaluate the ALP activity, cells were seeded in six-well tissue culture plates containing the fabricated films with a density of 1×10^5 cells at 37 °C. After 7 days of incubation, the adhered cells were gently rinsed with PBS and trypsinized. Then, the cells were lysed with 100 µl of Triton X-100 (1%). The cell lysate was centrifuged at 12000 rpm at 4 °C for 10 min to obtain a supernatant. Then, ALP activity was measured according to the manufacturer's instructions (Pars azmun ALP assay kit). The total protein concentration was determined using the Bradford assay. The activity of ALP was expressed as Unit per mg of protein.

2.9 Preparation of cell sample for FE-SEM photography

Cells were seeded in six-well tissue culture plates containing the fabricated films with a density of 1×10^5 cells at 37 °C. After the indicated time, the adhered cells were gently rinsed with PBS and fixed with glutaraldehyde 2.5% for 60 min. Cells were washed with PBS three times, and then dehydrated with graded ethanol series. The samples were coated with gold and then photographed with a field emission-scanning electron microscope.

2.10 Statistical analysis

In biological experiments, data are expressed as mean ± SD of three independent measurements and statistically analyzed using Student's t test. The experimental data were analyzed using ANOVA one-way analysis of variance and Tukey's post hoc test and p values ≤ 0.05 were considered significant.

3 Results

3.1 Sol stability

Sol stability is the critical factor for the provision of the uniform sol–gel coatings. To prepare a stable sol solution, the stability of the solutions was investigated at different pHs. For this purpose, the synthesis was performed with identical compositions at pH values of 0, 0.65, 2, 7, and 10, named S-pH 0, S-pH 0.65, S-pH 2, S-pH 7, and S-pH 10, respectively. Figure 1a shows the stability of the hydroxyapatite sol solution at different time points and pHs. According to the images, some precipitate and the semi-transparent solution appeared in S-pH 0.65, S-pH 2, S-pH 7, and S-pH 10 after 24 h of sol preparation. One week later, in S-pH 0.65, S-pH 2, S-pH 7, and S-pH 10 samples, the precipitation was completed (Fig. 1b). However, no precipitate was observed in the S-pH 0 solution and the solution remained completely transparent after a week. Therefore, the S-pH 0 solution was selected for the preparation of the hydroxyapatite coating on the surface of the substrate.
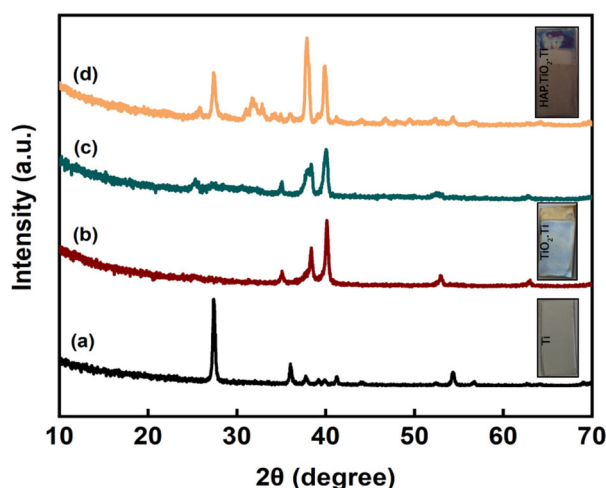
3.2 Phase characterization

In order to investigate the crystalline phase of the MHF and titania intermediate layer, XRD was used (Fig. 2).

The peaks located at $2\theta = 27.44$ °, 36.08°, 39.18°, 54.32°, and 62.74° can be indexed as (110), (101), (200), (211), and (220) crystalline planes, respectively. These peaks are related to the hexagonal crystal lattice of the pure titanium phase with lattice constants of $a = 4.593$ Å and
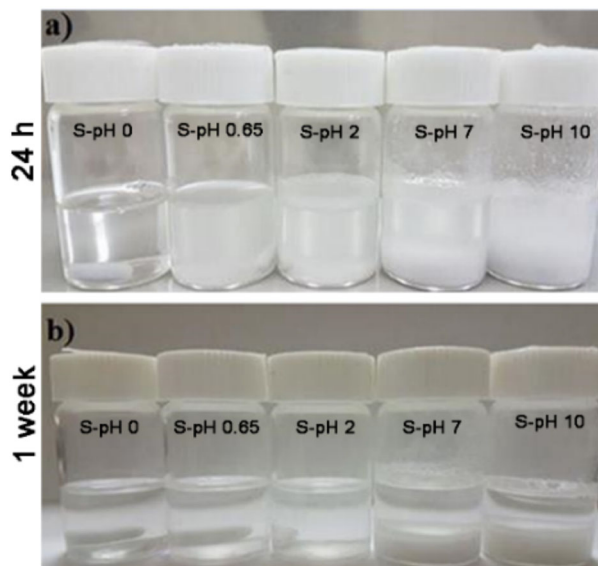
Fig. 1 Evaluation of the stability of the hydroxyapatite sol solution at different aging times and pHs. The sol stability after 24 h of aging (**a**) and after 1 week of aging (**b**)

Fig. 2 XRD patterns of **a** Ti substrate, **b** TiO$_2$ intermediate layer, **c** MHF500, and **d** MHF650, (inset: digital photographs of titanium substrate, titania coating on titanium substrate, and hydroxyapatite-titania double-layer coating on titanium substrate)

Table 1 The crystallite size and FWHM were estimated from the XRD pattern

Sample	FWHM (nm)	Crystallite size (nm)
MHAF350	0.4950	16.97
MHAF500	0.3188	26.54
MHAF650	0.3011	28.07

calcined film at 650 °C shows a higher crystallinity than the other coatings.

3.3 FTIR spectra

The formation and identification of the functional groups of mesoporous hydroxyapatite calcined at different temperatures were studied by FTIR (Fig. 3). In these spectra, the bands appearing in the approximate regions of 470, 563, and 602 cm^{-1} corresponded to the O–P–O bending vibrations in phosphate group.

The bands in regions of 960, 1033, and 1088 cm^{-1} were related to the stretching vibration of the phosphate group in the crystalline hydroxyapatite.

During the formation of hydroxyapatite, it is possible for other types of calcium phosphate phases to form; however, it depends on the synthesis conditions. In our experiment, for instance, the appearance of a small band at 872 cm^{-1} in the spectrum (b) and (c) was related to the carbonate group or a little amount of the HPO$_4^{-2}$ group (symmetric bending vibration of the P–O bond), implying a structural defect in the hydroxyapatite crystalline structure. Such defects arise from the high concentrations of hydrogen ions during the reaction when they are not completely removed from the structure of calcium phosphate. Interestingly, as the degree of crystallinity increased, the amount of carbonate impurity reduced. In fact, the existence of carbonate groups in the crystalline structure of hydroxyapatite reduces the crystallinity.

In the spectra, two broad bands appearing at 3421 and 1637 cm^{-1} are related to the stretching vibration of the hydroxyl group of adsorbed water on the hydroxyapatite surface. The absorption bands in 2877 and 2922 cm^{-1} are related to the CH$_2$ and CH groups, respectively, indicating the existence of a surfactant chain in the hydroxyapatite structure [48]. With increase in the calcination temperature, the intensity of these bands decreased, indicating an improvement in the decomposition of the surfactant.

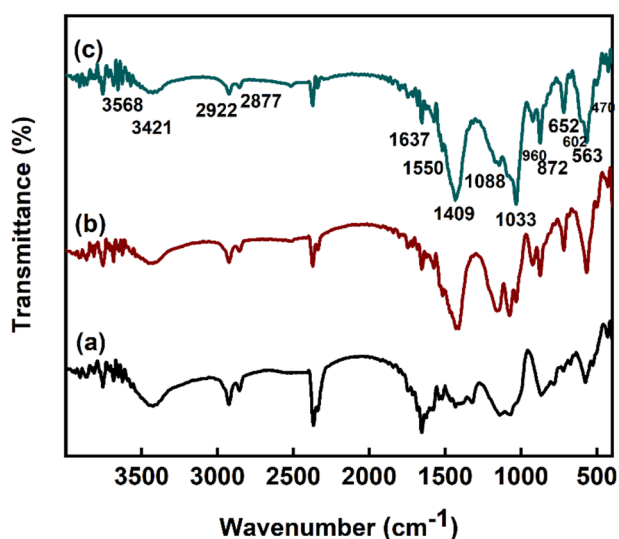### 3.4 Surface area and pore size distribution

To investigate the mesostructural characteristics of the coatings, nitrogen adsorption–desorption measurements were performed on the samples (Fig. 4).

All the samples show type IV isotherms with a distinct hysteresis loop (Fig. 4a), indicating the presence of a

$c = 2.959$ Å according to the 00-021-1276 PDF card number (Fig. 2a). The titania intermediate layer on the titanium substrate shows several diffraction peaks (Fig. 2b), and the strong peaks at $2\theta = 35.06°$, 38.40°, 40.15°, 53.01°, and 62.95° are in agreement with the 00-005-0682 PDF card number, which corresponds to the rutile phase with lattice constants of $a = 2.950$ Å and $c = 4.686$ Å, which can be indexed as (100), (002), (101), (102), and (110) crystalline planes, respectively. The rutile formation may be related to the chemical composition of the precursors, pH, and calcination cycle [45]. In addition, the titanium substrate may be involved in the formation of the rutile phase in the titania intermediate layer [46]. The MHF500 and MHF650 samples have the three strongest peaks at $2\theta = 25.9°$, 31.94°, and 32.24°. The observed peaks are diffracted from the planes with the index of (002), (211), and (300), respectively, matched with 01-074-0566 JCPDS card number for the hydroxyapatite phase (Fig. 2c, d) [47]. Despite the increase in temperature, no chemical reaction occurred between the coatings and the substrate. The lattice constants of hydroxyapatite with hexagonal crystal structure were determined as $a = 9.424$ Å and $c = 6.879$ Å. The XRD peaks of the MHF350 sample showed little intensity, indicating lowest crystallinity of hydroxyapatite at 350 °C calcination temperature (data not shown). To investigate the effect of calcination temperature on the crystallite size of the MHF materials, the size of crystallites was calculated by the Debye–Scherrer equation, using the (211) peak position. With respect to the calculated crystallite size value (Table 1), it was found that as calcination temperature increased, the size of the crystals augments from 16.97 to 28.07 nm. This increase reflects the grain growth and improvement of crystallinity of the coatings. According to the results, the

mesoporous structure; however, the mesopore size changed as a function of calcination temperature. As the calcination temperature increased, the beginning of the hysteresis loop occurred at a higher relative pressure (from 0.4 to 0.7 P/P$_0$). This shift is due to the enlargement of the mesopore diameter, which is confirmed by the pore size distribution curves.
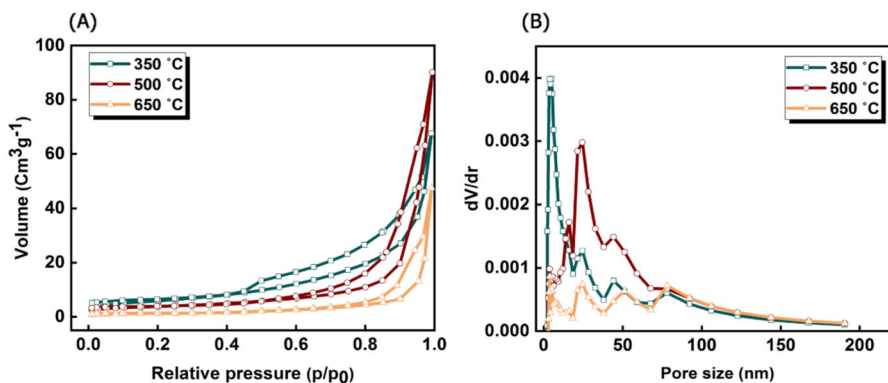
The pore size distribution of the fabricated samples was plotted according to the BJH method (Fig. 4b). It was evident that the pore diameter is dependent on the calcination temperature, ranging from 4 to 26 nm (Table 2).

Based on the BJH graphs, the heterogeneity in the pore size of MHF650 was detected, yet this did not occur in the MHF350 and MHF500 samples. Presumably, at a high calcination temperature (650 °C), pore wall is destroyed, leading to a wide range of pore sizes. In other words, pore size distribution could be manipulated by temperature. Furthermore, the surface area of the fabricated samples reduced as the temperature increased, which is likely due to the effect of heat treating on the pore network [49]. Following temperature enhancement, crystal grains became larger, leading to the agglomeration of the particles. Subsequently, the agglomeration of hydroxyapatite leds to the disappearance of pores at high temperatures. However, in the MHF350 sample, owing to the low calcination temperature, the crystals were not fully grown and empty spaces between them were created. Therefore, a disordered porous pattern was made by these empty spaces.

3.5 Chemical state of components

The chemical state of the elements was studied by the XPS technique. The study of the XPS spectrum shows the main elements of hydroxyapatite, Ca, P, O, and small amounts of contamination such as C (Fig. 5a). The XPS spectra of C1s, O1s, Ca2p, and P2p of the MHF650 are shown in Fig. 5b–e, and the binding energy values are summarized in Table 3. The binding energies were determined by reference to the C1s component due to carbon bond only to carbon or hydrogen, set at 285 eV [50]. The binding energy values of Ca2p and P2p are close to those values of hydroxyapatite in the NIST (National Institute of Standard and Technology) standard reference database.

The peak appearing in Fig. 5c at the binding energy values of 347.3 eV is attributed to the bonding between calcium and phosphorus ions in hydroxyapatite structure. The peak located at 531.3 eV in O1s spectra is attributed to the PO_3^{-4} group of hydroxyapatite [53, 54]. The binding energy values of Ca2p and P2p are located at 347.3 and

Fig. 3 The FTIR spectra of **a** MHF350, **b** MHF500, and **c** MHF650 samples

Table 2 Structural parameters of mesoporous hydroxyapatite thin films calcined at various temperatures

Sample	Pore volume (cm^3 g^{-1})	Pore diameter (nm)	Surface area (m^2 g^{-1})
MHAF350	0.1030	4.76	26.277
MHAF500	0.1310	24.49	15.038
MHAF650	6.8963	26.33	5.0940

The surface area, pore diameter, and pore volume of the samples obtained from nitrogen adsorption–desorption measurement

Fig. 4 N$_2$ adsorption–desorption isotherms (**a**) and pore size distribution curves (**b**) of MHF350, MHF500, and MHF650

Fig. 5 The XPS survey spectra of MHF650. **a** The XPS survey spectrum, **b–e** the high-resolution XPS spectra of P2p, Ca2p, O1s, and C1s, respectively
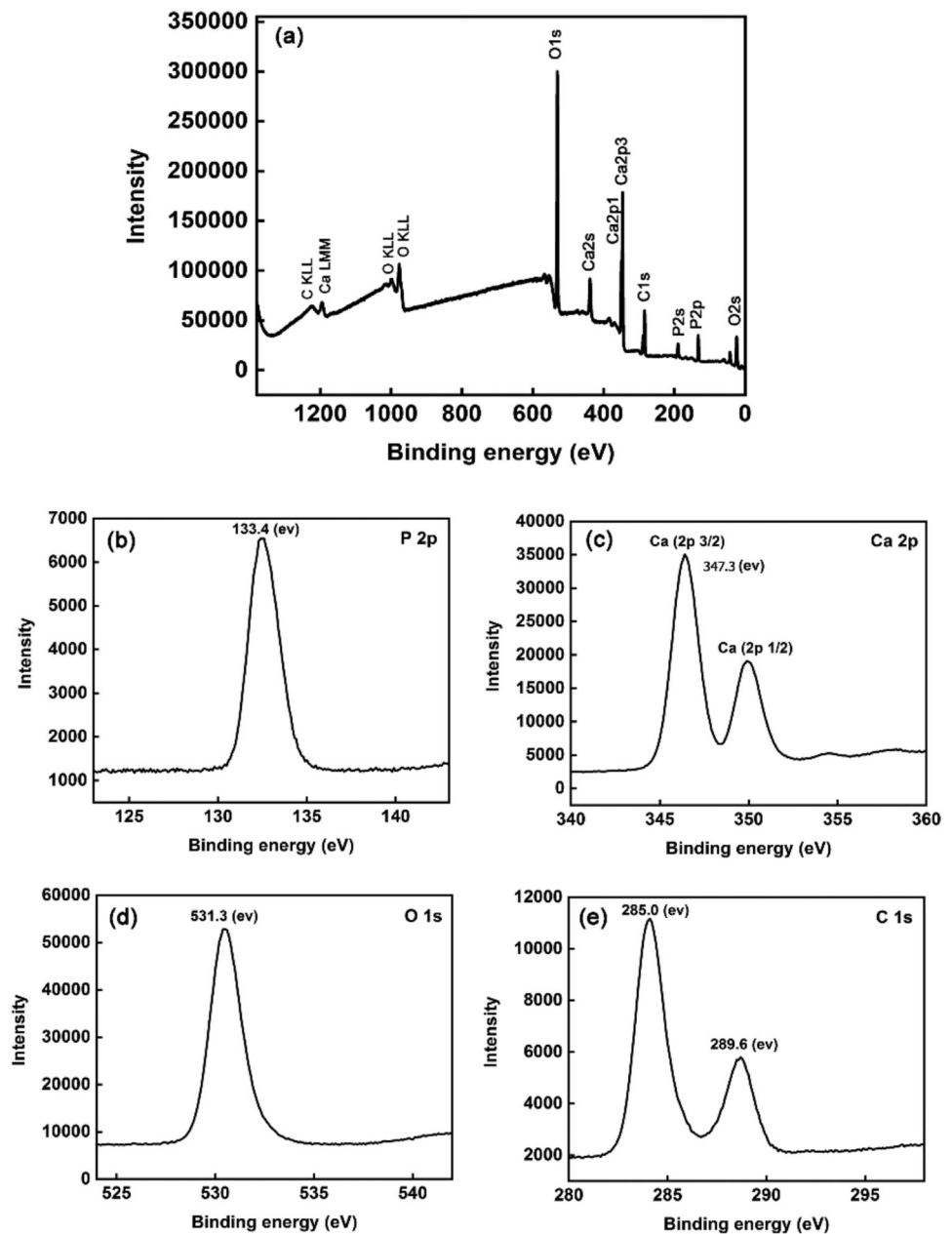
Table 3 Binding energy (BE) of the main XPS peaks of MHF650 sample and reference values for hydroxyapatite [29, 51, 52]

| Measured BE values of MHF650		Reference values [51, 52]
Ca 2p1/2	350.8	350.6–350.8
Ca 2p3/2	347.3	346.9–347.6
P2p	133.4	133.2–133.6
O1s	531.3	530–533

133.4 eV, respectively. Based on the XPS results, the chemical states of the components in the fabricated film are similar to those of ideal hydroxyapatite [55]. Moreover, the peak at 289.6 eV in the C1s curve is attributed to the CO_3^{-2} group of $CaCO_3$. Calcium carbonate is formed usually due to the presence of CO_2 and H_2O in the synthesis environment [29, 56].

3.6 Microstructure investigation

The surface, pore morphology, and microstructure properties of hydroxyapatite thin films were investigated by FE-SEM (Figs. 6 and 7).

As it can be seen in the top-view FE-SEM images, the coating surface is relatively smooth, continuous, and crack-free (Figs. 6a–f, 7a(a–e)). The low-resolution view
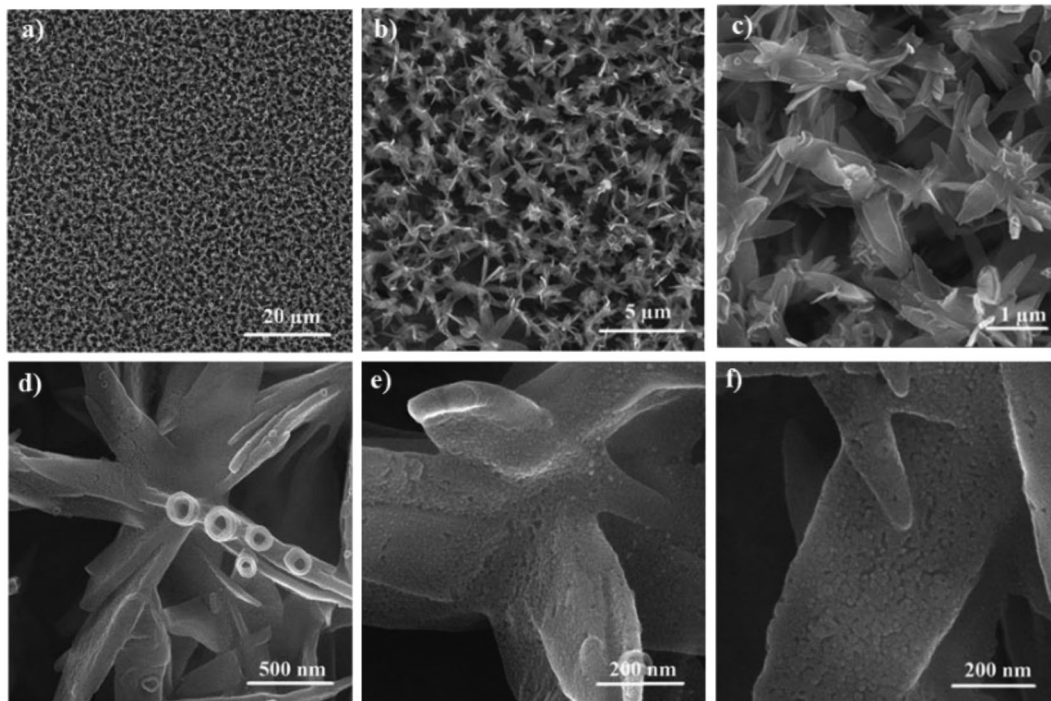
Fig. 6 FE-SEM images of MHF350 at low resolution (**a**, **b**, **c**) and high resolution (**d**, **e**, **f**)
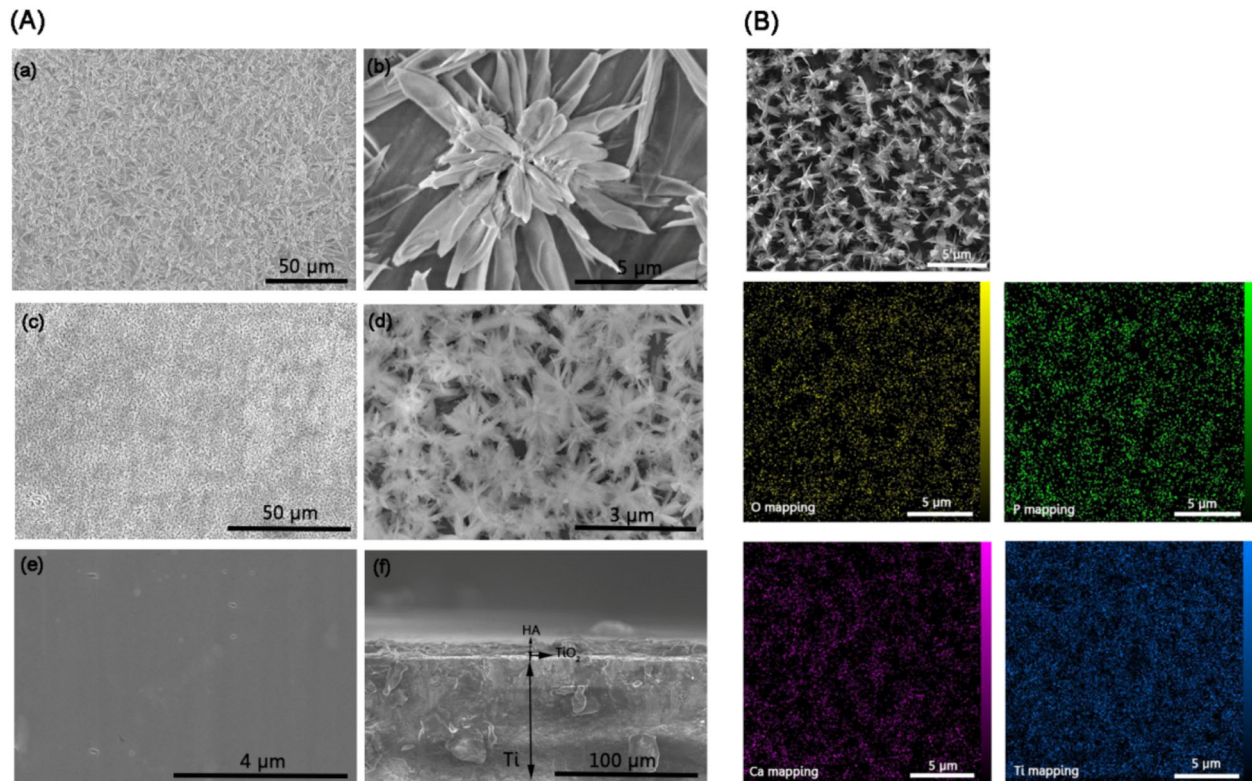
Fig. 7 FE-SEM images and elemental mapping of MHFs. **a** FE-SEM images of MHF500 (a, b), MHF650 (c, d), titania film (e), and cross-section image of the MHF/TiO$_2$ double-layer coating on the Ti substrate (f). **b** Elemental mapping of mesoporous hydroxyapatite film (MHF650) for O, P, Ca, and Ti elements

of the FE-SEM images shows hydroxyapatite films with flower-shaped morphology in different lengths and diameters. The flower-shaped morphology has been uniformly spread out over the entire area. The connections among flower-shaped structures have formed microporosity. Also, the images show the distribution of pores throughout the surface of coating and the presence of internal connections among the micropores (Fig. 6e, f and SI 1). Such porosity network makes hydroxyapatite film appropriate for biomedical applications [57]. Based on the high-resolution images, nanopores cover the entire surface. The mesoporous structure of hydroxyapatite is in a wide range from 2 to 20 nm, which is compatible with the BET analysis.

In addition, the surface morphology of the titania film is shown in Fig. 7e. The image shows that the coating surface is perfectly uniform and highly dense without any cracks. The titania film acts as an intermediate layer that eliminates the lattice mismatch between the Ti substrate and hydroxyapatite film, and improves the connection between them. Also, the cross-section image of the MHF on the Ti substrate was taken by FE-SEM (Fig. 7a(f)). According to the figure, the hydroxyapatite thin film and titania layer with nanometer thickness were formed on the Ti substrate. Both coatings were densely compact. A thickness of about 0.875 μm was measured for the smooth hydroxyapatite coating on the Ti substrate surface. The thickness value is significantly smaller than the other hydroxyapatite coatings created by sol–gel at a high pH value and plasma-spraying methods [58]. Further, the cross-section image reveals no interfacial debonding between the hydroxyapatite coating and the substrate.

The elemental distribution on the surface of the hydroxyapatite coating was determined by EDS and elemental mapping (Fig. 7b and SI 2). As shown in Fig. 7b, MAP analysis shows the presence of calcium, phosphorus, and titanium elements, which uniformly cover the entire surface with no aggregation in any part of the coating surface.

3.7 Surface properties

3.7.1 Evaluation of macrocrack formation

The surface properties of the coating were studied by COM (Fig. 8). It can be seen on the image that the titania layer (Fig. 8b) and hydroxyapatite (Fig. 8c) are formed well on the Ti substrate using the sol–gel method. No macrocrack was observed on the surface of the coating, which indicates an improvement of the adhesion of the hydroxyapatite coating to the Ti substrate, owing to the presence of titania intermediate layer.

### 3.7.2 Surface roughness and wettebility

To investigate the surface topography and roughness of the hydroxyapatite thin film on the Ti substrate, AFM analysis was performed (Fig. 9a). The images illustrate that in micrometer scales, the surfaces have convexities and concavities. The maximum height of the surface is 202 and 209.7 nm for the MHF650 and MHF500 samples, respectively. The topography of the surface showed that the surface of the MHF500 sample is more uniform than that of the MHF650 sample. Using the WSxM software, the values of the surface specification were extracted and are shown in Table 4. According to the rough mean square value, the MHF650 sample has a rougher surface than the MHF500 sample. To determine the formation of the film, the difference between the mean height and roughness was calculated. Note that smaller values mean a better feature of the film formation. Based on this analysis, the MHF650 sample has a better film formation than the MHF500 sample on the Ti substrate. Therefore, it can be concluded from the results of the AFM that the roughness of surface increases following the augmentation of crystallinity.

To evaluate the surface wettability of MHFs, the contact angles of ultrapure deionized water on the coating surface were determined (Fig. 9b). According to the images, the contact angle reduces by an increase in the calcination
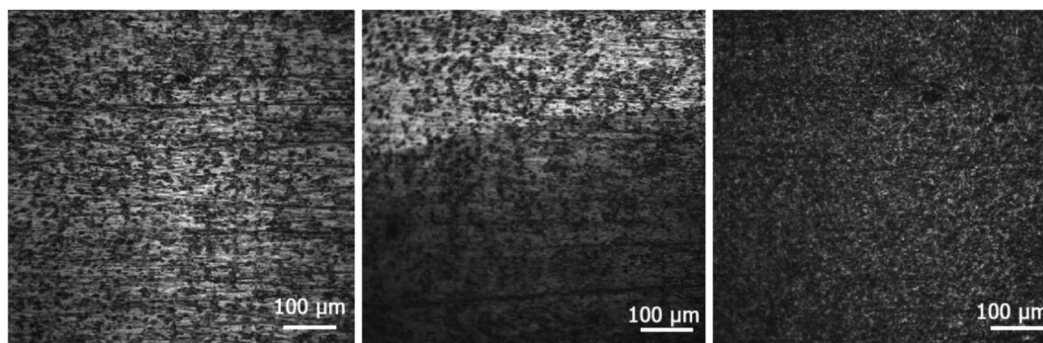
Fig. 8 COM images of **a** titania film, **b** TiO$_2$-coated substrate, and **c** mesoporous hydroxyapatite film

Fig. 9 a 3D AFM images of the (a) MHF650 and (b) MHF500 samples. **b** Water contact angle on (a) dense hydroxyapatite coating (without $C_{12}E_{10}$), (b) mesoporous hydroxyapatite film calcined at 500 °C, and (c) mesoporous hydroxyapatite film calcined at 650 °C
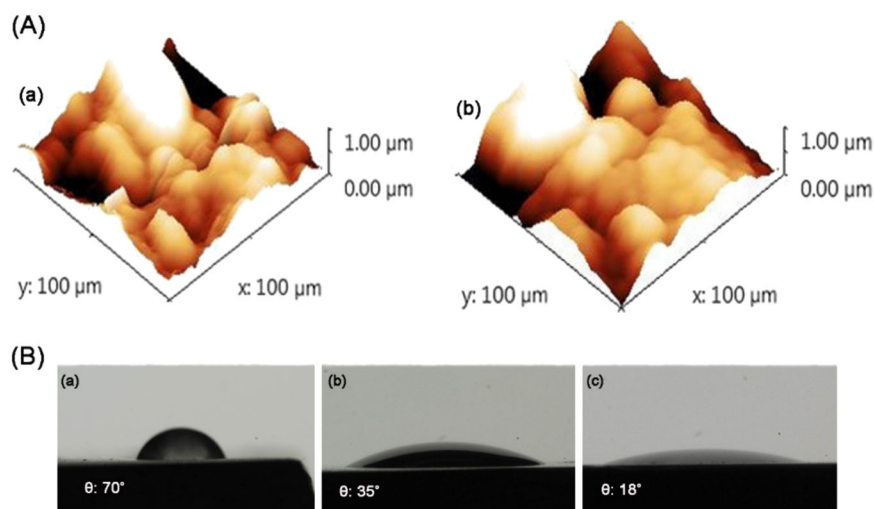
Table 4 Surface properties of MHF500 and MHF650 thin films

Sample	Roughness (nm)	Average height (nm)	RMS (nm)	Maximum height (nm)
MHF500	29	137	37	209.7
MHF650	34.66	92	41.8	202

temperature (up to 17° in the MHF650). This reduction in contact angle is due to the increase in hydrophilicity of the coating. The mesoporosity of the surface of the coating allows the penetration of water into the pores and the reduction of the surface energy between the surface and liquid, leading to a decrease in contact angle. In addition, the improvement of hydrophilicity of the film could be related to the presence of a hydroxyl group on the surface [59–61]. Increasing the hydrophilicity improves the biocompatibility of the surface, making the coating suitable for cell growth.

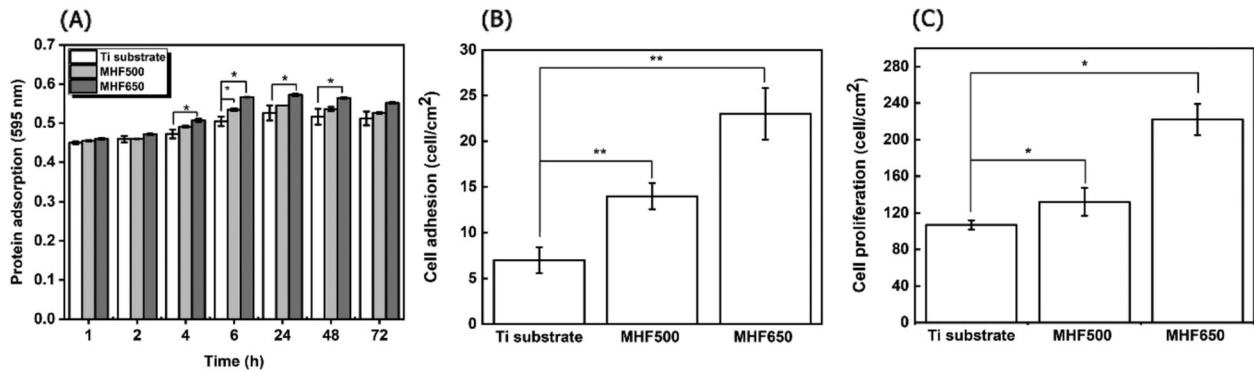### 3.8 Protein adsorption and cellular behavior of MSCs on MHFs

Protein adsorption on the surface of implants is the incipient biological step after implantation, acting as a signal for the migration of osteoblast cells and allowing implant osteointegration [62]. Therefore, the protein adsorption on the surface of the fabricated MHFs and Ti substrate was evaluated at different time intervals (2–72 h) at 37 °C. From the results presented in Fig. 10a, the protein adsorption increased on the surface of the implants in a time-dependent manner; however, a high level of protein adsorption was observed on the surface of the MHF materials in comparison to Ti substrate, which is likely related to the roughness topography of the sample [63].

To evaluate the adhesion of the MSCs onto the surface of the MHFs, the cells were seeded on the surface of the implants, and the number of the adhered cells were assessed after 4 h. As shown in Fig. 10b, the number of the adhered cells on the surface of the MHFs was significantly higher than that on the surface of the bare Ti substrate. The number of MSCs per mm^2 of MHF500 and MHF650 was 14 ± 1.4 and 23 ± 2.8 cell/cm^2, respectively, whereas this value decreased to 7 ± 1.4 cell/cm^2 for the bare substrate. The high tendency of the cells toward MHF650 may be attributed to the surface topography and wettability of the implant. It has previously been documented that a rough surface [64] with high hydrophilicity [65, 66] is more favorable for cell adhesion. As the proliferation of the progenitor cells is the first stage of osteogenesis, the proliferation of the adhered cells on the surface of the fabricated implants was evaluated after 7 days of incubation. As it is evident in Fig. 10c, a higher proliferation rate was observed in the MSCs cells incubated on the surface of MHF650 (222 ± 17 cell/cm^2) than those grown on the surface of MHF500 (132 ± 15 cell/cm^2) and the bare substrate (107 ± 5 cell/cm^2). In fact, MHF650 with interconnected macro-mesopores facilitates water and nutrient delivery, providing an appropriate surface for cell proliferation [67].
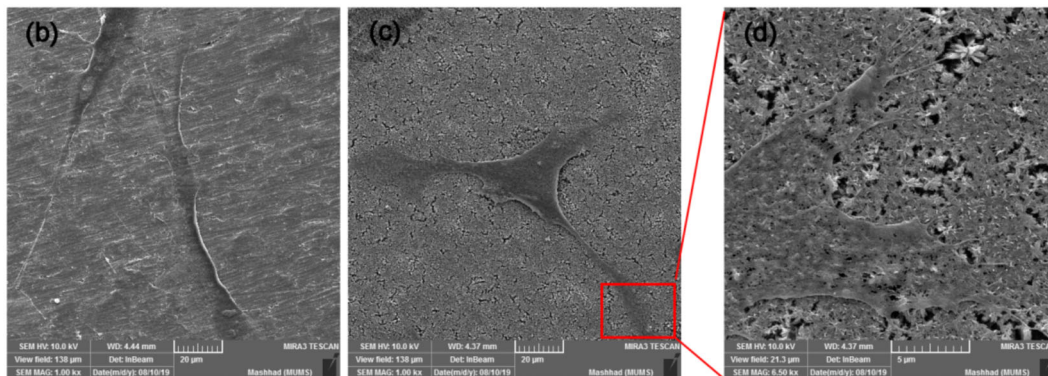
3.9 Assessment of ALP activity and morphological alteration

Regarding osteogenic differentiation, ALP activity is an essential indication of early stages of differentiation. It is considered as an important marker of osteogenesis [68]. Therefore, the osteogenic differentiation of the MSCs on the surface of the MHFs was monitored by the activity of ALP. As shown in Fig. 11a, a higher level of activity was observed in the MSCs grown on the surface of MHF650 (13.5 ± 1.5 unit/mg) than those cultured on the surface of MHF500 (10.2 ± 1.5 unit/mg) and the Ti bare substrate (6.9 ± 0.9 unit/mg), demonstrating the high capability of MHF650 in the induction of osteogenesis.

Fig. 10 Cellular behavior of MSCs on MHFs. **a** Protein adsorption behavior of MHFs at different time points (*$p < 0.05$). **b** Evaluation of cell adhesion and **c** proliferation of MSCs on the surface of MHFs after 4 h and 7 days of incubation, respectively (*$p < 0.05$, **$p < 0.01$). Each value represents the mean ± SD ($n = 3$)
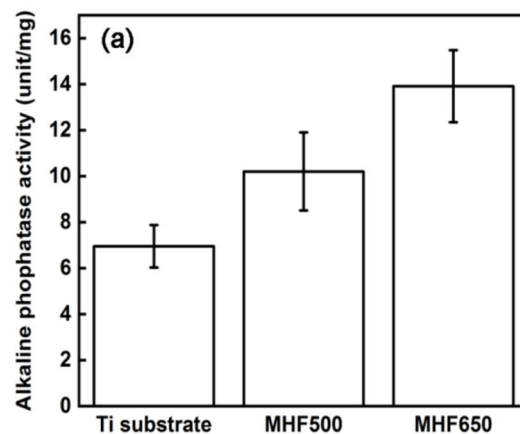
Fig. 11 Evaluation of osteogenic differentiation in MSCs induced by MHFs. **a** Assessment of ALP activity in MSCs incubated on the surface of fabricated sample for 7 days. FE-SEM images of MSCs morphology evaluation on the surface Ti substrate (**b**) and MHF650 (**c**). Fillopodia extruded from the MSC cultured on MHF650 (**d**)

Figure 11b–d shows the morphology of the MSCs cultured on the surface of MHF650 and the Ti substrate after 3 days of incubation. On the surface of MHF650, the cells exhibited a typical polygonal morphology and spread out with filopodium and lamellipodium; however, the cells displayed a spindle morphology as they grew on the surface of the Ti substrate. The results indicated that double-layer coating on the surface of Ti substrate significantly promotes osteogenesis.

4 Discussion

Bone-interfacing implants made from titanium alloy are widely used for both medical and dental implants. Initial implant stabilization, acceptable porous geometry, and the rapid establishment of osseointegration are critical factors for uninhibited bone ingrowth on the surface of the implant. To enhance the osteoconductivity of metallic implants,

several studies have suggested the effectiveness of hydroxyapatite surface coating [26, 27, 30, 58, 69], as it is the main constituent of hard tissues in the human body. In this line, there are wide varieties of methods for the deposition of hydroxyapatite on Ti alloy implants, such as plasma-spraying [70], laser interference patterning [71], and electrophoretic deposition [72].

In the plasma-spraying method, which is most often used for calcium phosphate coating, a thick layer (30–50 μm) consisting of hydroxyapatite and other phases is formed [73]. Owing to the significant structural defects in the coating-substrate interface introduced during coating application, delamination and detachment occur in physiological environment, leading to the liberation of particles and consequently promoting inflammation [74, 75]. In our study, we used the sol–gel technique, which is an ideal way for the creation of thin films owing to the phase homogeneity of the films, fine grain structure, low processing temperature, and effective production of the film on complex-shaped implants [26, 31, 41, 42]. However, this method is also accompanied by some disadvantages such as insufficient coating coherence and poor adhesion of hydroxyapatite to the Ti substrate, leading to the separation of the hydroxyapatite coating from the surface of the implant. Hence, HAP.Ti implants are inappropriate for long-term service in the human body. To address these issues, an intermediate layer like titania or zirconia has been introduced between hydroxyapatite and Ti substrate. The fabricated HAP.TiO$_2$.Ti implants are endowed with new physico-chemical and biological properties such as antibacterial activity. In this line, heat-treated Ti implants in the air or alkali-treated Ti implants were suggested for the formation of TiO$_2$ film on the surface of the Ti implant [76]. In the alkali-treated Ti implants, the TiO$_2$ intermediate layer is not monophasic, consisting of the sodium titanate (Na$_2$Ti$_5$O$_{11}$) and titanium dioxide. Note that in this method, controlling porous structure network and pore size of the TiO$_2$ layer is difficult. Special porous network, pore size with submicron scale, and the negatively charged titanium surface are required for the apatite nucleation [77]. In our study, the synthesis of TiO$_2$ was carried out through a simple procedure, sol–gel wet chemical precipitation route, which provides uniform and crack-free surface for the adhesion of hydroxyapatite. FE-SEM micrographs showed that the titania layer has been relatively well-incorporated in Ti substrate and hydroxyapatite layer, and no obvious separation was observed between them, indicating the strong bonding between the coatings and titanium substrate (Fig. 7a(f)). Therefore, it can be concluded that an intermediate layer eliminates the lattice mismatch between the metal substrate and the ceramic coating and improves adhesion between them.

Table 5 Summary of physico-chemical properties and biocompatibility of HAP-coated Ti alloy based on the coating method

Sample	HAP coating Method	Morphology of HAP	Porosity	Biological evaluation	Comment	Reference
HAP.TiO$_2$.Ti	Sol–gel	Flower-like nanocrystals	Macro-mesoporous (based on SEM images and BET analysis)	Protein adsorption Cell adhesion and proliferation assay Evaluation of osteogenesis	Improved bioactivity (protein adsorption, cell adhesion and proliferation and osteogenesis) of Ti implant by tuning of precursor molar ratio, calcination temperature, and pH	This study
HAP.TiO$_2$.Ti	Sol–gel	Amorphous HAP	ND	Cell proliferation assay	Improved cellular response	[81]
HAP.Ti CaTiO$_3$.Ti	Sol–gel	Amorphous HAP	Porous surface (Based on SEM images)	–	–	[69]
HAP.Ti	Plasma-spraying	Amorphous HAP	ND	SBF assay	–	[75]
HAP.Ti	Inductively coupled radio frequency (RF) plasma spray	Amorphous HAP	ND	Protein release assay Bone formation assay in vivo study	Enhanced in vivo osteogenesis of Ti implant	[27]
Ag.HAP.Ti	Sol–gel	Amorphous HAP	ND	Antimicrobial tests	Improved antibacterial properties	[26]
Sr.HAP.Ti	Radio frequency (RF) magnetron co-sputtering	Amorphous HAP	ND	–	–	[58]

SBF simulated body fluid, ND not determined

In addition, the synthesis of the hydroxyapatite layer with special morphology (flower-like) and dual porosity system (meso-macro porous) using a nonionic diblock copolymer template provides a more favorable surface for cell adhesion and proliferation. Among different samples, MHF650 showed higher roughness and wettability; consequently, the cells showed a high tendency toward MHF650 than other MHFs. Note that it has previously been reported that an implant with a rough surface has a favorable effect on early and strong bonding to bone [78–80]. Moreover, the surface chemistry and wettability are critical parameters on protein and cell adhesion, as cells live in a chemistry-rich microenvironment. It has been documented that the improvement of hydrophilicity of the film could be related to the presence of hydroxyl and phosphate groups on the surface of the implant, regulating the conformation of the initial adsorbed protein and the subsequent behavior of the adhered cells [65, 66]. Such desirable chemistry was also detected on the surface of the fabricated MHF samples. To exhibit the outstanding points in our study, we summarized previous reports related to physico-chemical properties and biocompatibility of HAP-coated Ti substrate in Table 5.

5 Conclusion

In this study, the MHFs on the titanium substrate have been successfully prepared by the sol–gel dip-coating method. Owing to the weak adhesion of the hydroxyapatite coating to the metal substrate, TiO_2 was used as an intermediate layer, eliminating the lattice mismatch between the Ti substrate and hydroxyapatite film. Physico-chemical analysis indicated the synthesis of macro-mesoporous hydroxyapatite, exploiting a nonionic surfactant, $C_{12}E_{10}$. The synthesis procedure was optimized in a highly acidic environment at different temperatures, leading to the formation of hydroxyapatite with flower-like morphology. Based on in vitro cellular assay, MHF650 showed better biocompatibility and osteogenic behavior in terms of cellular adhesion, proliferation, and differentiation than the other fabricated samples. This may be related to its favorable properties such as interconnected macro-mesoporous structure, rough topography, and wettability as compared with those of the other fabricated samples. According to these results, MHF650 has a great potential for repairing and regenerating bone tissues; however, more experiments are still required to establish the in vitro and in vivo efficacy of this biomaterial.

Compliance with ethical standards

Conflict of interest The authors declare that they have no conflict of interest.

Publisher's note Springer Nature remains neutral with regard to jurisdictional claims in published maps and institutional affiliations.

References

1. Oveisi H, Beitollahi A, Imura M, Wu CW, Yamauchi Y. Synthesis and characterization of highly ordered titania-alumina mixed oxide mesoporous films with high alumina content. Microporous Mesoporous Mater. 2010;134:150–6.

2. Imani A, Oveisi H. 3D-ordered mesoporous chromium-doped titania thin films: the effect of metal dopant on the microstructure, mesoporous symmetry, hydrophobicity, and surface properties. ChemistrySelect. 2018;3:4586–92.

3. Li T, Shi S, Goel S, Shen X, Xie X, Chen Z, et al. Recent advancements in mesoporous silica nanoparticles towards therapeutic applications for cancer. Acta Biomater. 2019;89:1–13.

4. Ibrahim M, Labaki M, Giraudon JM, Lamonier JF. Hydroxyapatite, a multifunctional material for air, water and soil pollution control: a review. J Hazard Mater. 2020;383:121139.

5. Oveisi H, Rahighi S, Jiang X, Nemoto Y, Beitollahi A, Wakatsuki S, et al. Unusual antibacterial property of mesoporous titania films: drastic improvement by controlling surface area and crystallinity. Chem Asian J. 2010;5:1978–83.

6. Zirak M, Oveisi H, Lin J, Bando Y, Alshehri AA, Kim J, et al. Synthesis of CdS/ZnO hybrid nanoarchitectured films with visible photocatalytic activity. Bull Chem Soc Jpn. 2018;91:1556–60.

7. Feiz MS, Meshkini A. Targeted delivery of adenosine 5′-triphosphate using chitosan-coated mesoporous hydroxyapatite: a theranostic pH-sensitive nanoplatform with enhanced anti-cancer effect. Int J Biol Macromol. 2019;129:1090–102.

8. Zhang J, Fujiwara M, Xu Q, Zhu Y, Iwasa M, Jiang D. Synthesis of mesoporous calcium phosphate using hybrid templates. Microporous Mesoporous Mater. 2008;111:411–6.

9. Zhang L, Jin L, Liu B, He J. Templated growth of crystalline mesoporous materials: from soft/hard templates to colloidal templates. Front Chem. 2019;7:22–22.

10. Oveisi H, Rahighi S, Jiang X, Agawa Y, Beitollahi A, Wakatsuki S, et al. Improved inactivation effect of bacteria: fabrication of mesoporous anatase films with fine Ag nanoparticles prepared by coaxial vacuum arc deposition. Chem Lett. 2011;40:420–2.

11. Zhao Y, Ma J, Tan GEB. Synthesis of mesoporous hydroxyapatite through neutral templating. Int J Nanosci. 2006;5:499–503.

12. Lalzawmliana V, Anand A, Roy M, Kundu B, Nandi SK. Mesoporous bioactive glasses for bone healing and biomolecules delivery. Mater Sci Eng C. 2019;106:110180.

13. Sistanipour E, Meshkini A, Oveisi H. Catechin-conjugated mesoporous hydroxyapatite nanoparticle: a novel nano-antioxidant with enhanced osteogenic property. Colloids Surfaces B. 2018;169:329–39.

14. Harun WSW, Asri RIM, Alias J, Zulkifli FH, Kadirgama K, Ghani SAC, et al. A comprehensive review of hydroxyapatite-based coatings adhesion on metallic biomaterials. Ceramics Int. 2018;44:1250–68.

15. Turon P, del Valle LJ, Alemán C, Puiggalí J. Chapter 2—Grafting of hydroxyapatite for biomedical applications. In: Thakur VK, editor. Biopolymer grafting. Elsevier; 2018. p. 45–80.

16. Behnamsani A, Meshkini A. Synthesis and engineering of mesoporous ZnO@HAP heterostructure as a pH-sensitive nano-

photosensitizer for chemo-photodynamic therapy of malignant tumor cells. J Drug Delivery Sci Technol. 2019;53:101200.

17. Meshkini A, Oveisi H. Methotrexate-F127 conjugated mesoporous zinc hydroxyapatite as an efficient drug delivery system for overcoming chemotherapy resistance in osteosarcoma cells. Colloids Surfaces B. 2017;158:319–30.

18. Mohd Pu'adNAS, Koshy P, Abdullah HZ, Idris MI, Lee TC. Syntheses of hydroxyapatite from natural sources. Heliyon. 2019;5:e01588.

19. Yang Y, Wu Q, Wang M, Long J, Mao Z, Chen X. Hydrothermal synthesis of hydroxyapatite with different morphologies: influence of supersaturation of the reaction system. Cryst Growth Des. 2014;14:4864–71.

20. Jeong J, Kim JH, Shim JH, Hwang NS, Heo CY. Bioactive calcium phosphate materials and applications in bone regeneration. Biomater Res. 2019;23:4.

21. Su Y, Cockerill I, Zheng Y, Tang L, Qin YX, Zhu D. Biofunctionalization of metallic implants by calcium phosphate coatings. Bioactive Mater. 2019;4:196–206.

22. Niinomi M. Mechanical biocompatibilities of titanium alloys for biomedical applications. J Mech Behav Biomed Mater. 2008;1:30–42.

23. Kaur M, Singh K. Review on titanium and titanium based alloys as biomaterials for orthopaedic applications. Mater Sci Eng C. 2019;102:844–62.

24. Zhang LC, Chen LY. A review on biomedical titanium alloys: recent progress and prospect. Adv Eng Mater. 2019;21:1801215.

25. Kumar A, Biswas K, Basu B. Hydroxyapatite-titanium bulk composites for bone tissue engineering applications. J Biomed Mater Res. 2015;103:791–806.

26. Batebi K, Abbasi Khazaei B, Afshar A. Characterization of sol-gel derived silver/fluor-hydroxyapatite composite coatings on titanium substrate. Surf Coat Technol. 2018;352:522–8.

27. Vahabzadeh S, Roy M, Bandyopadhyay A, Bose S. Phase stability and biological property evaluation of plasma sprayed hydroxyapatite coatings for orthopedic and dental applications. Acta Biomater. 2015;17:47–55.

28. He D, Liu P, Liu X, Ma F, Chen X, Li W, et al. Characterization of hydroxyapatite coatings deposited by hydrothermal electrochemical method on NaOH immersed Ti6Al4V. J Alloys Compd. 2016;672:336–43.

29. Hsieh MF, Perng LH, Chin TS. Hydroxyapatite coating on Ti6Al4V alloy using a sol–gel derived precursor. Mater Chem Phys. 2002;74:245–50.

30. Kim HW, Koh YH, Li LH, Lee S, Kim HE. Hydroxyapatite coating on titanium substrate with titania buffer layer processed by sol-gel method. Biomaterials. 2004;25:2533–8.

31. Kim HW, Kim HE, Knowles JC. Improvement of hydroxyapatite sol–gel coating on titanium with ammonium hydroxide addition. J Am Ceram Soc. 2005;88:154–9.

32. Huang Y, Yan Y, Pang X. Electrolytic deposition of fluorine-doped hydroxyapatite/ZrO2 films on titanium for biomedical applications. Ceram Int. 2013;39:245–53.

33. Kim HW, Kim HE, Salih V, Knowles JC. Hydroxyapatite and titania sol–gel composite coatings on titanium for hard tissue implants; Mechanical and in vitro biological performance. J Biomed Mater Res Part B. 2005;72B:1–8.

34. He X, Zhang G, Wang X, Hang R, Huang X, Qin L, et al. Biocompatibility, corrosion resistance and antibacterial activity of TiO2/CuO coating on titanium. Ceram Int. 2017;43:16185–95.

35. Basavarajappa PS, Patil SB, Ganganagappa N, Reddy KR, Raghu AV, Reddy CV. Recent progress in metal-doped TiO2, non-metal doped/codoped TiO2 and TiO2 nanostructured hybrids for enhanced photocatalysis. Int J Hydrogen Energy. 2020;45:7764–78.

36. Patil SB, Basavarajappa PS, Ganganagappa, Jyothi MS, Raghu AV, Reddy KR. Recent advances in non-metals-doped TiO2 nanostructured photocatalysts for visible-light driven hydrogen production, CO2 reduction and air purification. Int J Hydrogen Energy. 2019;44:13022–39.

37. Ravindra C, Deepak K, Shilpa N, Saraswati M, Anand N. Design of eco-friendly PVA/TiO2-based nanocomposites and their antifungal activity study. Green Mater. 2020;8:40–8.

38. Oveisi H, Jiang X, Nemoto Y, Beitollahi A, Yamauchi Y. Cerium-doped mesoporous TiO2 thin films: controlled crystallization of anatase with retention of highly ordered mesostructure. Microporous Mesoporous Mater. 2011;139:38–44.

39. Vaquila I, Vergara L, Passeggi M Jr, Vidal R, Ferron J. Chemical reactions at surfaces: titanium oxidation. Surf Coat Technol. 1999;122:67–71.

40. Dieudonne S, Van Den Dolder J, De Ruijter J, Paldan H, Peltola T, Van't Hof M, et al. Osteoblast differentiation of bone marrow stromal cells cultured on silica gel and sol–gel-derived titania. Biomaterials. 2002;23:3041–51.

41. Brinker CJ, Hurd AJ, Schunk PR, Frye GC, Ashley CS. Review of sol-gel thin film formation. J Non-Cryst Solids. 1992;147:424–36.

42. Sakka S. Preparation and properties of sol-gel coating films. J Sol-Gel Sci Technol. 1994;2:451–5.

43. Oveisi H, Suzuki N, Nemoto Y, Srinivasu P, Beitollahi A, Yamauchi Y. Critical effect of aging condition on mesostructural ordering in mesoporous titania thin film. Thin Solid Films. 2010;518:6714–9.

44. Ernst O, Zor T. Linearization of the bradford protein assay. J Vis Exp. 2010;38:1918.

45. Hanaor DAH, Sorrell CC. Review of the anatase to rutile phase transformation. J Mater Sci. 2011;46:855–74.

46. Ghaith ES, Hayakawa T, Kasuga T, Nogami M. Apatite formation on rutile type TiO2 films formed by laser irradiation. J Mater Sci. 2006;41:2521–4.

47. Tunkara E, Dag Ö. Salt-acid-surfactant lyotropic liquid crystalline mesophases: synthesis of highly transparent mesoporous calcium hydroxyapatite thin films. Eur J Inorg Chem. 2016;2016:2114–21.

48. Salimi E, Javadpour J, Anbia M. Template-based synthesis of nanoporous hydroxyapatite. ISRN Ceram. 2012;2012:1–6.

49. Adell R, Lekholm U, Rockler B, Brånemark PI. A 15-year study of osseointegrated implants in the treatment of the edentulous jaw. Int J Oral Surg. 1981;10:387–416.

50. Maachou H, Genet MJ, Aliouche D, Dupont-Gillain CC, Rouxhet PG. XPS analysis of chitosan–hydroxyapatite biomaterials: from elements to compounds. Surf Interface Anal. 2013;45:1088–97.

51. Chusuei CC, Goodman DW, Van Stipdonk MJ, Justes DR, Schweikert EA. Calcium phosphate phase identification using XPS and time-of-flight cluster SIMS. Anal Chem. 1999;71:149–53.

52. Kačiulis S, Mattogno G, Pandolfi L, Cavalli M, Gnappi G, Montenero A. XPS study of apatite-based coatings prepared by sol–gel technique. Appl Surf Sci. 1999;151:1–5.

53. Wagner CD. NIST X-ray photoelectron spectroscopy database, NIST Standarad Reference Database 20. 2000.

54. Chetibi L, Hamana D, Achour S. Growth and characterization of hydroxyapatite nanorice on TiO2 nanofibers. Mater Chem Phys. 2014;144:301–9.

55. Yamaguchi T, Tanaka Y, Ide-Ektessabi A. Fabrication of hydroxyapatite thin films for biomedical applications using RF magnetron sputtering. Nucl Instrum Methods Phys Res Sect B. 2006;249:723–5.

56. Lu HB, Campbell CT, Graham DJ, Ratner BD. Surface characterization of hydroxyapatite and related calcium phosphates by XPS and TOF-SIMS. Anal Chem. 2000;72:2886–94.

57. Zhang J, Liu G, Wu Q, Zuo J, Qin Y, Wang J. Novel mesoporous hydroxyapatite/chitosan composite for bone repair. J Bionic Eng. 2012;9:243–51.

58. Boyd AR, Rutledge L, Randolph LD, Meenan BJ. Strontium-substituted hydroxyapatite coatings deposited via a co-deposition sputter technique. Mater Sci Eng C. 2015;46:290–300.

59. Suhas DP, Aminabhavi TM, Raghu AV. para-Toluene sulfonic acid treated clay loaded sodium alginate membranes for enhanced pervaporative dehydration of isopropanol. Appl Clay Sci. 2014;101:419–29.

60. Suhas DP, Aminabhavi TM, Jeong HM, Raghu AV. Hydrogen peroxide treated graphene as an effective nanosheet filler for separation application. RSC Adv. 2015;5:100984–95.

61. Suhas DP, Aminabhavi TM, Raghu AV. Mixed matrix membranes of H-ZSM5-loaded poly(vinyl alcohol) used in pervaporation dehydration of alcohols: influence of silica/alumina ratio. Polym Eng Sci. 2014;54:1774–82.

62. Agarwal R, García AJ. Chapter 37—surface modification of biomaterials. In: Atala A, Lanza R, Mikos AG, Nerem R, editors. Principles of regenerative medicine. 3rd ed. Boston: Academic Press; 2019. p. 651–60.

63. Akkas T, Citak C, Sirkecioglu A, Güner FS. Which is more effective for protein adsorption: surface roughness, surface wettability or swelling? Case study of polyurethane films prepared from castor oil and poly(ethylene glycol). Polym Int. 2013;62:1202–9.

64. Feller L, Jadwat Y, Khammissa RAG, Meyerov R, Schechter I, Lemmer J. Cellular responses evoked by different surface characteristics of intraosseous titanium implants. Biomed Res Int. 2015;2015:171945.

65. Hao L, Fu X, Li T, Zhao N, Shi X, Cui F, et al. Surface chemistry from wettability and charge for the control of mesenchymal stem cell fate through self-assembled monolayers. Colloids Surfaces B. 2016;148:549–56.

66. Yu M, Gong J, Zhou Y, Dong L, Lin Y, Ma L, et al. Surface hydroxyl groups regulate the osteogenic differentiation of mesenchymal stem cells on titanium and tantalum metals. J Mater Chem B. 2017;5:3955–63.

67. Zhang R, Elkhooly TA, Huang Q, Liu X, Yang X, Yan H, et al. Effects of the hierarchical macro/mesoporous structure on the osteoblast-like cell response. J Biomed Mater Res Part A. 2018;106:1896–902.

68. Li N, Zhou L, Xie W, Zeng D, Cai D, Wang H, et al. Alkaline phosphatase enzyme-induced biomineralization of chitosan scaffolds with enhanced osteogenesis for bone tissue engineering. Chem Eng J. 2019;371:618–30.

69. Usinskas P, Stankeviciute Z, Beganskiene A, Kareiva A. Sol-gel derived porous and hydrophilic calcium hydroxyapatite coating on modified titanium substrate. Surface Coat Technol. 2016;307:935–40.

70. Junker R, Manders PJ, Wolke J, Borisov Y, Jansen JA. Bone-supportive behavior of microplasma-sprayed CaP-coated implants: mechanical and histological outcome in the goat. Clin Oral Implants Res. 2010;21:189–200.

71. Surmeneva M, Nikityuk P, Hans M, Surmenev R. Deposition of ultrathin nano-hydroxyapatite films on laser micro-textured titanium surfaces to prepare a multiscale surface topography for improved surface wettability/energy. Materials. 2016;9:862.

72. Suo L, Jiang N, Wang Y, Wang P, Chen J, Pei X, et al. The enhancement of osseointegration using a graphene oxide/chitosan/hydroxyapatite composite coating on titanium fabricated by electrophoretic deposition. J Biomed Mater Res Part B: Appl Biomater. 2019;107:635–45.

73. Lacefield WR. Current status of ceramic coatings for dental implants. Implant Dent. 1998;7:315–22.

74. Radin Ducheyne P. Plasma spraying induced changes in calcium phosphate ceramic characteristics and the effect on in vitro stability. J Mater Sci Mater Med. 1992;3:33–42.

75. Rakngarm Nimkerdphol A, Otsuka Y, Mutoh Y. Effect of dissolution/precipitation on the residual stress redistribution of plasma-sprayed hydroxyapatite coating on titanium substrate in simulated body fluid (SBF). J Mech Behav Biomed Mater. 2014;36:98–108.

76. Liang F, Zhou L, Wang K. Apatite formation on porous titanium by alkali and heat-treatment. Surface Coat Technol. 2003;165:133–9.

77. Wen HB, de Wijn JR, Cui FZ, de Groot K. Preparation of calcium phosphate coatings on titanium implant materials by simple chemistry. J Biomed Mater Res. 1998;41:227–36.

78. Deligianni DD, Katsala N, Ladas S, Sotiropoulou D, Amedee J, Missirlis YF. Effect of surface roughness of the titanium alloy Ti–6Al–4V on human bone marrow cell response and on protein adsorption. Biomaterials. 2001;22:1241–51.

79. Deligianni DD, Katsala ND, Koutsoukos PG, Missirlis YF. Effect of surface roughness of hydroxyapatite on human bone marrow cell adhesion, proliferation, differentiation and detachment strength. Biomaterials. 2000;22:87–96.

80. Sharafipour M, Oveisi H, Meshkini A. Meso-macroporous crack-free nanohydroxyapatite coatings templated by C12E10 diblock copolymer on Ti6Al4V implant materials toward human osteoblast-like cells. J Biomed Mater Res Part A. 2020;108:882–94.

81. Kim HW, Koh YH, Li LH, Lee S, Kim HE. Hydroxyapatite coating on titanium substrate with titania buffer layer processed by sol–gel method. Biomaterials. 2004;25:2533–8.